BIOINSPIRED COMPLIANT LIMBS FOR ROBUST LANDING OF FREE-FLYING ROBOTS

Jane Pauline Ramirez[1], **Anton Bredenbeck**[1], **and Salua Hamaza**[1]

[1]*Biomorphic Intelligence Lab, Dept. of Control & Operations, Faculty of Aerospace Engineering, TU Delft*
J.P.RRamirez@tudelft.nl

ABSTRACT

Traditional landing gear consists of rigid linkages with dampers. They require a flat surface to function. In unstructured environments such as lunar craters or the martian polar region, these conditions are not always met. In this work, we equip a conventional quadrotor with four continuously deformable passive landing limbs with a logarithmic spiral geometry. By choosing the right geometric design as well as tension on the tendon running through the length of the limbs, we ensure that the limbs support the overall weight while passively complying to the environment. Hence, no active control during the landing process is needed in order to adapt to irregular ground. In a set of experiments, these compliant limbs showcase their ability to adjust to uneven landing terrain while maintaining the horizontal attitude of the base vehicle. Overall, this work highlights the future potential to access more challenging environments, leveraging physical compliance for robust landings.

1. INTRODUCTION

Human presence on non-terrestrial bodies has attracted sustained interest over the years. An ongoing program that caters to this objective is ARTEMIS [1]. It aims to reestablish human presence in the moon, therefore the need for robotic solutions for exploration is necessary. They have been proven to be one of the key enablers in the past to take on risky tasks. Most recent successful robots are the Curiosity [2] and Perseverance [3] rovers, and the Ingenuity [4] helicopter. In the future, robotic systems have the potential to help prepare for long-term human presence on the surface of the moon and even on other celestial bodies.

One of the significant challenges in transporting these robotic systems into the location of interest is the landing procedure. Landing on uneven terrain is particularly challenging [5]. Robotic moon landers use thrusters as propulsion due to the lack of atmosphere. Thrusters inherently provide a unidirectional force. Hence, to move in the lateral direction, the system has to rotate such that the thrusters provide a lateral force component. This coupling of Degrees-of-Freedom (DoFs) is called "underactuation" and results in a lack of control authority in the lateral direction while landing horizontally. Landing on uneven ground causes tilting, and the lack of control authority increases the possibility of landing failure which can lead to the failure of the whole mission.

Figure 1: A conventional quadrotor equipped with passively deforming landing gear demonstrates the ability to comply with uneven terrain allowing the main body to maintain a vertical attitude. Each of the four landing arms adjusts the shape to match the environment by deforming passively according to the external forces.

In this work, we show the role of compliant landing gear in allowing systems to handle rough terrain passively. By embodying intelligence in the physical design of the landing gear, the system is resilient to landing shock. It dampens vibrations during landing and adapts to uneven terrain without the need

for active control. To showcase these capabilities, we design a bio-inspired compliant limb with adjustable stiffness characteristics as pictured in figure 1. As proof of concept, we further mount the landing gear on an underactuated quadrotor. We then execute various drop tests to showcase the system's capability to maintain a horizontal orientation throughout the landing procedure.

2. DESIGN

Drawing inspiration from the gripper design of Wang et al. [6], this work proposes to use a logarithmic spiral geometry, typically found in nature [7], for the design of the compliant limbs. This design allows curling adaptation of the mechanism's longitudinal length to unknown terrain topology, and object shapes. In its fully curled state, its description in polar coordinates – its radius r as a function of the angle ϕ – defines the spiral as:

$$r = ae^{k\phi}, \quad \phi \in \mathbb{R}, \quad a > 0, \quad k \neq 0. \tag{1}$$

where a and k are its amplitude and pitch, respectively. Here, we manufacture the compliant structure in a monolithic fashion, without using an intermediate elastic layer, exploiting the flexible material's properties. This significantly simplifies the manufacturing process as it allows for full-structure printing.

2.1. Fabrication

The design of each landing limb prioritizes passive compliance and makes them nearly continuously deformable. The structure material was then chosen to be thermoplastic urethane (shore hardness of 95A, density of 1 g/cm^3). The employed filament is vacuum dried for nine hours at 70°C. Mounting structures were made of polylactic acid for ease and speed of printing.

We use two 1.2 mm ultra-high molecular weight polyethylene cords for the tendons. Each limb has two tendons in distal lateral ends running through a tapered straight line along its length. The tendons provide the possibility to pretension the limb to a desired configuration. Besides the material characteristics, the effective cartesian stiffness of the limbs is also dependent on its current configuration. Thus, the pre-tension of the tendons allows for fine-tuning the limbs' stiffness for the overall system mass. A render of the CAD model is in figure 2.

2.2. Characterization

We characterize the newly manufactured structure using a 20 N Zwick Static Test Machine to understand the relation between the force applied to the tendon and the End-Effector (EE) displacement. The tendon attached to one side of the structure is put under tension in the fully neutral position. Figure 3 shows the resulting hysteresis loop of stiffening the tendon and releasing it. Between 10 N to 60 N we observe a linear relation, thus, for the sake of conciseness, the rest of this work only considers this restricted range.

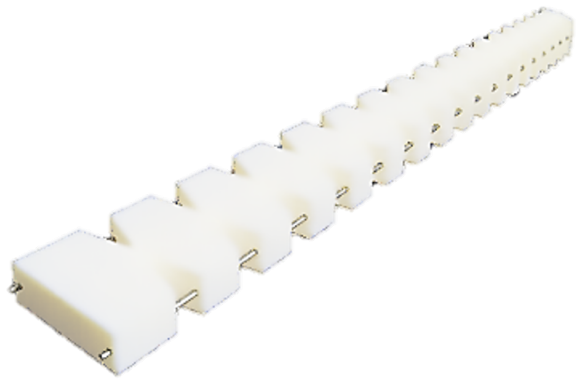

Figure 2: Render of the fabricated limb.

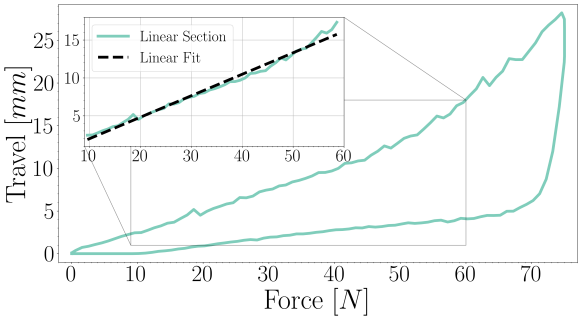

Figure 3: Force-tendon travel graph of a newly manufactured structure. The peak force is experienced when the tip is on the same level of the base.

2.3. Component Sizing

The employed quadrotor (Holybro X500 V2) has a payload capacity of 1 kg. With a generous safety margin, we assume that 60% of this will be used for onboard computer and other electronic components needed for flight. Hence, there is a 400 g allowance for the limb assembly, amounting to 100 g per limb assembly. Table 1 shows the resulting specifications.

3. MODELLING

Pulling the tendon creates tension on the lateral sides of the structure, applying bending moments on the pivot points of each unit along the frontal midline of the structure. These result in stresses that change

Table 1: System Specifications

Quadrotor Model	Holybro X500 V2
Payload Capacity	$\sim$1 kg
All-up-weight	1012.8 g (w/o battery)
Limb Weight	$51.20 \times 4 = 204.8$ g
Limb & mountings	$95.45 \times 4 = 381.8$ g

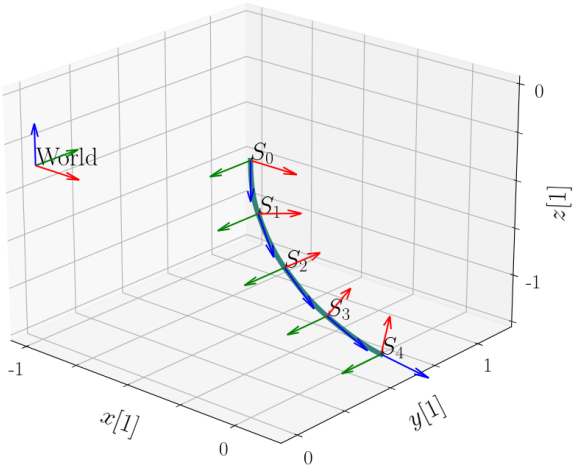

Figure 4: An example of a piecewise-affine curve description. Each reference frame S_i is connected via an affine curve.

the configuration, which consequently increases the effective cartesian stiffness in the EE. To choose a desired tendon tension this section proposes a model that relates said tendon tension to the limb configuration, as well as limb configuration to EE stiffness. We propose to model the limbs using techniques from continuum robotics, i.e., model the limb as a concatenation of n piecewise affine curves – curves of linearly changing curvature – as introduced in [8] and [9].

3.1. Forward Kinematics

The base reference frame S_0 is followed by one reference frame at the tip of each segment S_i as depicted in figure 4.

Since the limbs are inextensible and only bend in one axis, each segment i is fully determined by its curvature c_i. For each actuated segment, we choose one affine description of the curvature in the form of

$$c_i(s) = c_{i;0} + c_{i;1}s, \tag{2}$$

where $s \in [0, 1]$ parametrizes the position along the arc length of the segment. The bending angle α_i at some arc length s along the segment with respect to the previous frame is then the integral of the curvature

$$\alpha_i(s) = \int_0^s c_i(s) = c_{i;0}s + \frac{c_{i;1}}{2}s^2, \tag{3}$$

The overall configuration $\mathbf{q} \in \mathbb{R}^{2n}$ is then fully defined by the description of the limb's curvature

$$\mathbf{q} = [c_{0;0} \quad c_{0;1} \quad \cdots \quad c_{n;0} \quad c_{n;1}], \tag{4}$$

The forward kinematics - the EE position $\mathbf{r}$ as a function of the configuration variables - then follow as in [9]:

$$\mathbf{FK}(\mathbf{q}) = \mathbf{H}\left(\Pi_{i=1}^{n}\mathbf{T}_{i-1}^{i}(\mathbf{q})\right), \tag{5}$$

where $\mathbf{T}_{i-1}^{i}(\mathbf{q})$ is the homogeneous transformation matrix of reference frame S_i with respect to reference frame S_{i-1} and $\mathbf{H}$ is the (linear) transformation of the homogeneous coordinates to cartesian coordinates.

3.2. The Jacobian

The systems EE-Jacobian $\mathbf{J}(\mathbf{q})$ is a matrix collecting all partial derivatives of the forward kinematics:

$$\mathbf{J}(\mathbf{q}) = \begin{bmatrix} \frac{\partial \mathbf{r}}{\partial q_{0;0}} & \frac{\partial \mathbf{r}}{\partial q_{0;1}} & \cdots & \frac{\partial \mathbf{r}}{\partial q_{n;0}} & \frac{\partial \mathbf{p}}{\partial q_{n;1}} \end{bmatrix}, \tag{6}$$

where $\mathbf{r}$ denotes the EE position in cartesian space with respect to the base reference frame. Using the Jacobian we can derive a simplified dynamical system under the influence of actuation and gravity.

3.3. Dynamics

In general, the Partial Differential Equation (PDE) that fully describes the behavior of a robotic system takes on the form of the manipulator equation, following the Lagrangian formalism:

$$\begin{aligned} \mathbf{M}(\mathbf{q})\ddot{\mathbf{q}} + \mathbf{C}(\mathbf{q}, \dot{\mathbf{q}})\dot{\mathbf{q}} + \mathbf{D}(\mathbf{q})\dot{\mathbf{q}} \\ + \mathbf{G}(\mathbf{q}) + \mathbf{K}(\mathbf{q}) = \mathbf{A}(\mathbf{q})\boldsymbol{\tau} \end{aligned} \tag{7}$$

where $\mathbf{M}(\mathbf{q})$ is the system's mass-inertial matrix, $\mathbf{C}(\mathbf{q}, \dot{\mathbf{q}})$ collects the Coriolis terms, $\mathbf{D}(\mathbf{q})$ the damping terms, and $\mathbf{G}(\mathbf{q})$,$\mathbf{K}(\mathbf{q})$, the gravity and stiffness terms respectively while $\mathbf{A}(\mathbf{q})$ maps the control input into generalized forces on the states. However, in this work, the focus is on the steady-state configurations of the system, i.e., $\dot{\mathbf{q}} = 0$ and $\ddot{\mathbf{q}} = 0$. In steady state, the following simpler equation holds:

$$\mathbf{G}(\mathbf{q}) + \mathbf{K}(\mathbf{q}) = \mathbf{A}(\mathbf{q})\boldsymbol{\tau} \tag{8}$$

I.e., to fully define the steady state equation under a given tendon tension, only the $\mathbf{G}$, $\mathbf{K}$, and $\mathbf{A}$ need to

be known. First, we derive $\mathbf{K}$. The potential energy stored in the stiffness of a segment is

$$U_{E;i} = \int_0^1 \frac{k}{2} c_i^2(s) ds \tag{9}$$

where k is the stiffness constant of the material and is assumed to be constant along the arc length. Forming the derivative with respect to the state yields the stiffness contribution $\mathbf{K}(\mathbf{q})$ onto the state

$$\mathbf{K}_i(\mathbf{q}) = \frac{d}{d\mathbf{q}} U_{E:i} = \underbrace{k \begin{bmatrix} 1 & 1/2 \\ 1/2 & 1/3 \end{bmatrix}}_{\mathbf{K}_i = \text{const}} \mathbf{q} \tag{10}$$

where in the rest of this work the constant factor in front of the state is referred to as $\mathbf{K}_i$. Furthermore, we derive the gravity contribution $\mathbf{G}(\mathbf{q})$ by summing up the contributions of all infinitesimal components of a segment

$$\mathbf{G}(\mathbf{q}) = \int_0^1 \rho(s) \mathbf{J}^T(\mathbf{q}, s) \mathbf{g} ds \tag{11}$$

$$\approx \sum_{i=0}^{k} \frac{m}{k} \mathbf{J}^T(\mathbf{q}, s) \mathbf{g} \tag{12}$$

where ρ is the material density, $\mathbf{J}(\mathbf{q}, s)$ is the jacobian at arc length s, $\mathbf{g}$ is the gravitational acceleration vector, m is the total mass, and k is the number of discrete points used to approximate the integral numerically.

Lastly, the actuation mapping $\mathbf{A}(\mathbf{q}) \in \mathbb{R}^{2 \times n}$ follows the derivation in [10] of a torque acting on the tip of the segment and results in

$$\mathbf{A}(\mathbf{q}) = \begin{bmatrix} 1 & \cdots & 1 \\ \frac{1}{2} & \cdots & \frac{1}{2} \end{bmatrix} \tag{13}$$

Albeit being simpler, equation 8 is transcendental and, in general, has no closed-form solution for $\mathbf{q}$. As proposed in [9], we introduce a damping term to form the following dynamic function that allows us to simulate the system until convergence:

$$\dot{\mathbf{q}} = \mathbf{D}_*^{-1} \left(\mathbf{A}(\mathbf{q}) \boldsymbol{\tau} - \mathbf{G}(\mathbf{q}) + \mathbf{K}(\mathbf{q}) \right) \tag{14}$$

where $\mathbf{D}_*$ is an arbitrary damping matrix, heuristically chosen to yield fast convergence. Note that equation (14) yields the same steady-state as equation 8.

Since each of the designed limbs is equipped with one tendon, it is sufficient to model and simulate the limbs with one affine curve segment. Figure 5 showcases a selection of the steady-state configurations of a single-segment model for various constant control inputs.

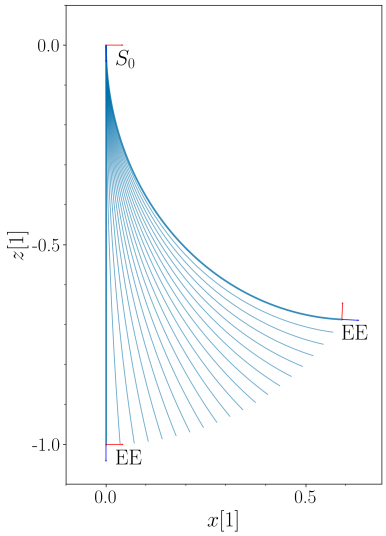

Figure 5: Various steady state configurations of a single segment affine curve continuum robot of unit length for ten constant control inputs $\mathbf{u} = [0, \cdots, u_{max}]$N m.

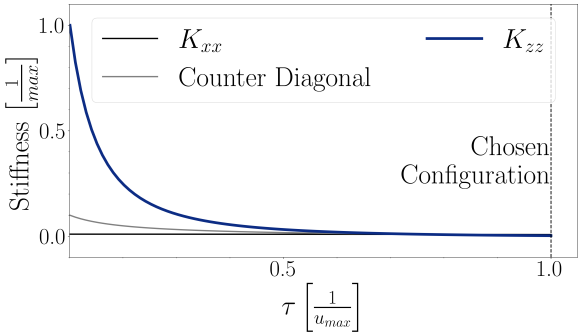

Figure 6: Elements of the cartesian stiffness matrix of the EE, normalized to its maximal value, in different steady-state configurations given various constant control inputs $\mathbf{u}$. The dashed line indicates the chosen configuration.

3.4. Effective cartesian stiffness

While the bending stiffness of the continuum arm is modeled as a constant, the resulting cartesian stiffness of the EE depends on the limb configuration $\mathbf{q}$. At any given configuration, the resulting EE stiffness matrix in cartesian space $\mathbf{K}_C$ is

$$\mathbf{K}_C(\mathbf{q}) = \left(\mathbf{J}(\mathbf{q}) \mathbf{K} \mathbf{J}^T(\mathbf{q}) \right)^{-1} \tag{15}$$

Figure 6 showcases the elements of the resulting stiffness matrix in various steady-state configurations under the influence of constant control inputs.

For the purpose of compliant landing, we choose the configuration with minimal stiffness in z, which still permits the configuration to be such that the EE is

Table 2: Trials and Failures during each experiment

Configuration	Trials	Failures
Landing Gear No Object	12	5
Landing Gear Object	10	10
Limbs No Object	10	0
Limbs Gear Object	13	0

the lowest point of the limb. Figure 6 indicates the chosen configuration. Note that this is also the last simulated configuration in figure 5.

4. RESULTS

To validate their capability to adjust to uneven ground, we subject the system to repeated drop tests.

As illustrated in figure 7, the compliant landing gear deforms around the uneven ground topology while maintaining a close to horizontal orientation of the base, whereas the conventional landing gear fails to adapt and causes the system to tip over.

Figure 8 shows the roll, pitch, and system height over repeated drop tests from one meter height on a flat ground, as well as with an object. We consider a landing a failure if the system tips over during the landing process, i.e., reaches a steady state with a roll or pitch angle of more than 45°. Table 2 displays the number of trials and failures for each of the configurations. The system with conventional landing gear fails in 42% of the trials on flat ground and in 100% of the trials with the object. On the other hand, the system with compliant landing gear fails in none of the trials throughout all experiments.

Since the compliant limbs deform during the landing, they further dissipate energy, i.e., given the same impact velocity, the system with compliant landing gear is decelerating over a longer period, thus experiencing smaller peak accelerations. In the experimental setup, the rigid landing gear is longer than the compliant landing gear, thus striking the ground earlier while reaching a lower maximal velocity. However, when comparing the maximum velocity to peak acceleration ratio over all non-object trials, we observe a decrease of 33% percent. This implies that at the same impact velocity, the compliant landing gear reduces the experienced peak acceleration by a third.

5. CONCLUSION

This work proposes to use compliant landing gear in order to increase the robustness of landing maneuvers of airborne, underactuated robotic systems, such as planetary landers. This work introduces the design of bio-inspired compliant limbs and models them as an affine curve, actuated by one fixed tendon that provides tension to the system. By varying the tension of the tendons, the configuration and consequently the system's cartesian stiffness at the EE can be tuned to fit the requirements of the landing procedure. As proof of concept, we mount these limbs on a similarly underactuated quadrotor and perform a set of drop tests. It shows that the compliant limbs adapt to the uneven environment in each trial while the conventional landing gear fails and tips over in all trials with an object and 40% of the trials on flat ground. Furthermore, this work shows that, given the same impact velocity, the designed landing gear reduces the experienced peak acceleration by a third.

In future work, additional tendons in each limb would allow to not only tune the stiffness at the EE in one configuration but to shape the curve of stiffness elements throughout the entire landing process. These tendons could then be fixed to keep the system fully passive but could also be driven by actuators to adjust the stiffness online, such as the aerial compliant manipulators in [11, 12].

REFERENCES

1. M. Smith, D. Craig, N. Herrmann, E. Mahoney, J. Krezel, N. McIntyre, and K. Goodliff, "The artemis program: An overview of nasa's activities to return humans to the moon," in *2020 IEEE Aerospace Conference*, pp. 1–10, 2020.

2. R. Welch, D. Limonadi, and R. Manning, "Systems engineering the curiosity rover: A retrospective," in *2013 8th International Conference on System of Systems Engineering*, pp. 70–75, 2013.

3. N. Mangold, S. Gupta, O. Gasnault, G. Dromart, J. Tarnas, S. Sholes, B. Horgan, C. Quantin-Nataf, A. Brown, S. Le Mouélic, *et al.*, "Perseverance rover reveals an ancient delta-lake system and flood deposits at jezero crater, mars," *Science*, vol. 374, no. 6568, pp. 711–717, 2021.

4. J. Balaram, M. Aung, and M. P. Golombek, "The ingenuity helicopter on the perseverance rover," *Space Science Reviews*, vol. 217, no. 4, p. 56, 2021.

5. H. Paul, R. Miyazaki, R. Ladig, and K. Shimonomura, "Landing of a multirotor aerial vehicle on an uneven surface using multiple on-board manipulators," in *2019 IEEE/RSJ International Conference on Intelligent Robots and Systems (IROS)*, pp. 1926–1933, 2019.

6. Z. Wang and N. M. Freris, "Bioinspired soft spiral robots for versatile grasping and manipulation," *arXiv preprint arXiv:2303.09861*, 2023.

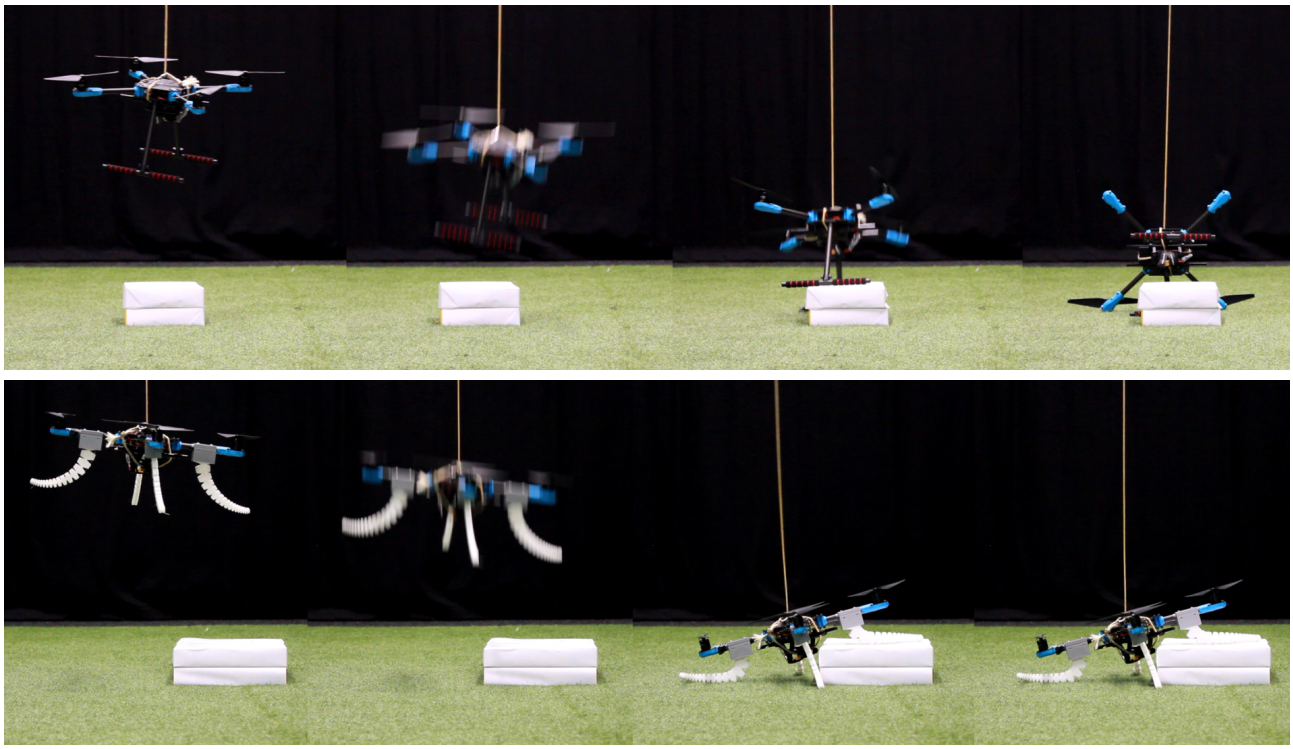

Figure 7: Drop tests with conventional, rigid (top) and compliant (bottom) landing gear. The compliant landing gear adjusts to the environment and enables successful landing, whereas the landing with the conventional landing gear fails.

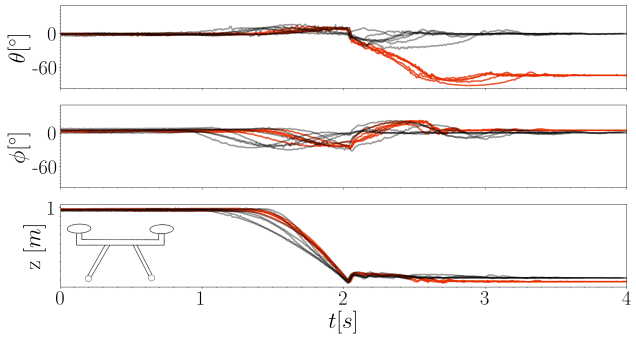

(a) Conventional Landing Gear, Flat Ground

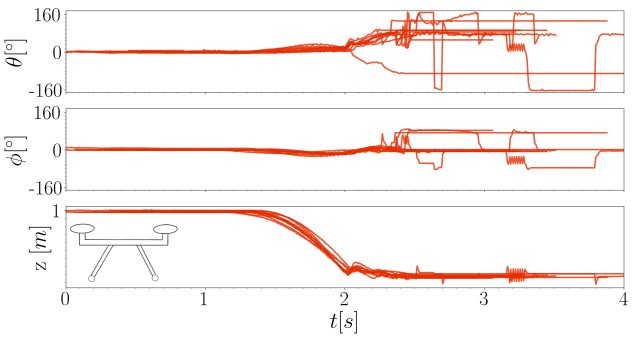

(b) Conventional Landing Gear, Object

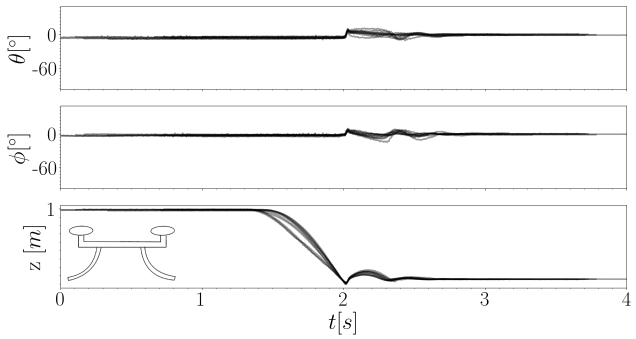

(c) Compliant Landing Gear, Flat Ground

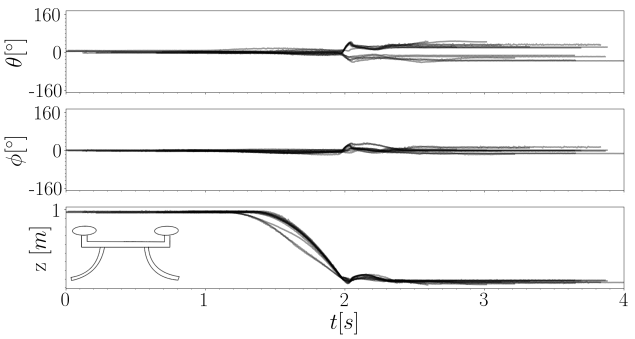

(d) Compliant Landing Gear, Object

Figure 8: Drop tests with conventional landing gear as well as with the compliant landing gear. Figures 8a and 8b show the tests with conventional landing gear with even and uneven ground, respectively. Figures 8c and 8d show the same for the compliant landing gear. Trials that resulted in a landing failure (Pitch or Yaw angle over 45° at steady state) are colored in red.

7. G. Harary and A. Tal, "The natural 3d spiral," in *Computer Graphics Forum*, vol. 30, pp. 237–246, Wiley Online Library, 2011.

8. C. D. Santina, "The soft inverted pendulum with affine curvature," in *2020 59th IEEE Conference on Decision and Control (CDC)*, pp. 4135–4142, 2020.

9. F. Stella, Q. Guan, C. Della Santina, and J. Hughes, "Piecewise affine curvature model: a reduced-order model for soft robot-environment interaction beyond pcc," in *2023 IEEE International Conference on Soft Robotics (RoboSoft)*, pp. 1–7, 2023.

10. C. D. Santina and D. Rus, "Control oriented modeling of soft robots: The polynomial curvature case," *IEEE Robotics and Automation Letters*, vol. 5, no. 2, pp. 290–298, 2020.

11. S. Hamaza, I. Georgilas, and T. Richardson, "An adaptive-compliance manipulator for contact-based aerial applications," in *2018 IEEE/ASME International Conference on Advanced Intelligent Mechatronics (AIM)*, pp. 730–735, IEEE, 2018.

12. S. Hamaza, I. Georgilas, and T. Richardson, "Towards an adaptive-compliance aerial manipulator for contact-based interaction," in *2018 IEEE/RSJ International Conference on Intelligent Robots and Systems (IROS)*, pp. 1–9, IEEE, 2018.